Multispectral Remote Sensing of the Earth and Environment Using KHawk Unmanned Aircraft Systems

By

Saket Gowravaram

Submitted to the Graduate Degree Program in Aerospace Engineering and the Graduate Faculty

of the University of Kansas in partial fulfillment of the requirements

for the degree of Master of Science in Aerospace Engineering.

_____

Chair: Dr. Haiyang Chao

_____

Dr. Nathaniel Brunsell

_____

Dr. Dongkyu Choi

Date Defended: 20 July 2017

The thesis committee for Saket Gowravaram certifies that this is the approved

version of the following thesis:

Multispectral Remote Sensing of the Earth and Environment

Using KHawk Unmanned Aircraft Systems

_____

Chair: Dr. Haiyang Chao

_____

Dr. Nathaniel Brunsell

_____

Dr. Dongkyu Choi

Date Approved: 27 July 2017

Abstract

This thesis focuses on the development and testing of the KHawk multispectral remote sensing system for environmental and agricultural applications. KHawk Unmanned Aircraft System (UAS), a small and low-cost remote sensing platform, is used as the test bed for aerial video acquisition. An efficient image geotagging and photogrammetric procedure for aerial map generation is described, followed by a comprehensive error analysis on the generated maps. The developed procedure is also used for generation of multispectral aerial maps including red, near infrared (NIR) and colored infrared (CIR) maps. A robust Normalized Difference Vegetation index (NDVI) calibration procedure is proposed and validated by ground tests and KHawk flight test. Finally, the generated aerial maps and their corresponding Digital Elevation Models (DEMs) are used for typical application scenarios including prescribed fire monitoring, initial fire line estimation, and tree health monitoring.

Acknowledgments

Table of Contents

List of Figures

List of Tables

Acronyms

AGL   Above Ground Level

CIR   Color Infrared

CST   Central Standard Time

CUSL   Cooperative Unmanned Systems Laboratory

dB   Decibel

DEM   Digital Elevation Model

DN   Digital Number

EPP   Expanded Polypropylene

FOV   Field of View

GCP   Ground Control Point

GCS   Ground Control Station

GPS   Global Positioning System

HFOV   Horizontal Field of View

IMU   Inertial Measurement Unit

LANDSAT   Land Remote Sensing Satellite (System)

LASE   Low altitude short endurance

LIDAR   Light Detection and Ranging

NDVI   Normalized Difference Vegetation Index

NIR   Near Infrared

p   Pixel

RADAR   Radio Detection and Ranging

RGB   Red, Green and Blue

RTK   Real Time Kinematic

SAR   Synthetic Aperture Radar

SLAR   Side Looking Airborne Radars

UAS   Unmanned Aircraft System

UTM   Universal Transverse Mercator

1 Introduction

1.1 Thesis Roadmap

This thesis focuses on the development and testing of the KHawk multispectral remote sensing system for environmental and agricultural applications. Multispectral remote sensing has many applications including soil status analysis, vegetation detection, crop growth mapping, and disaster damage tracking, etc. The use of UASs as remote sensing platforms have become very popular over the years due to their easy handling qualities. With the development of high-quality cameras and sensors, UASs can produce accurate and reliable measurements of the Earth at very high spatial and temporal resolutions (cm level). However, there are several challenges for UAS based remote sensing including small footprint coverage, missing standard calibration procedures, and high weather dependency. This thesis presents our approach for the generation of high-quality multispectral aerial maps using KHawk UASs. The proposed aerial mapping system can support both digital images and videos, which is ideal for monitoring of fast evolving processes such as wildfires. Another important contribution of this thesis is the development of a robust NDVI calibration procedure, which is crucial for accurate NDVI calculation.

1.2 Background

1.2.1 History of Remote Sensing

The technology of modern remote sensing began with the invention of the camera more than 150 years ago. The possibility of estimating the properties of the Earth and the environment without making physical contact paved way for a vast range of applications in various fields including geography, Earth sciences, military, urban planning, agriculture, etc. The earliest applications of remote sensing date back to the 1840s when balloons were used to capture still images for the purposes of topographic mapping [1]. By the First World War, the use of cameras

1

on aircraft for military purposes became very popular which led to the standardization of aerial photography as a tool for surface depiction. During the 1950s, multispectral images (mainly, visible, near infrared) became widely accepted for the identification of different vegetation types and analysis of vegetation growth [2]. Earth Observing satellites like the LANDSAT provides a vast majority of multispectral data sets, which are used for the study of land, vegetation trends, water and soil quality and numerous other earth science problems [3]. However, satellite based remote sensing systems have their own limitations such as the difficulty of localization, relatively low update rates, and mid-level resolutions.

1.2.2 Multispectral Remote Sensing

Multispectral remote sensing is defined as the collection of reflected, emitted or backscattered rays from an object or area of interest in multiple bands of the electromagnetic spectrum including visible, infrared, near infrared and thermal bands, microwave and radio wave bands. There are many applications of multispectral imagery including soil status analysis, vegetation detection, crop growth mapping, disaster damage tracking, soil-water interaction, etc.

The development of multispectral based vegetation indices has paved the way for many of the above applications. A vegetation index is a spectral transformation of two or more bands designed to quantify the contribution of vegetation properties [4]. The most commonly used multispectral vegetation indices are:

- Normalized Difference vegetation index (NDVI).

- Soil-Adjusted Vegetation index (SAVI).

- Enhanced Vegetation index (EVI).

Each of these indices operate in different ways. For instance, the NDVI is mostly used to detect the presence and health of crop canopies in a field using the red and near infrared spectral

bands [5]. SAVI, is an improved version of the NDVI, which minimizes the soil moisture brightness influences from spectral vegetation indices involving the red and near infrared bands [6]. EVI is designed to enhance the vegetation signal with improved sensitivity in high biomass regions and improved vegetation monitoring through a de-coupling of the canopy background signal and a reduction in atmosphere influences with the use of red, blue and the near infrared bands [7].

1.2.3 Unmanned Aircraft Systems

An Unmanned Aircraft System (UAS) comprises of a remotely piloted aircraft and the ground control station [8]. A UAS platform can be controlled remotely or operated autonomously based on a pre-planned flight trajectory or real time navigation system. Since its inception, UAS has become a major contributor to various applications, including aerial reconnaissance, agricultural monitoring, military surveillance and disaster management. The evolution of UAS technology, over the years, has paved the way for its inclusion into the fields of remote sensing and photogrammetry. UAS platforms have various advantages over manned aircraft and satellites, such as low cost, easy handling qualities, and high flexibility. They also have the capability to produce high-quality aerial imagery with desired pixel resolutions.

1.2.4 UAS Remote Sensing Platforms and Payloads

The most important components in any UAS based remote sensing mission are the platform characteristics and sensing payloads. Aerial image/video acquisition, image geotagging and photogrammetric procedures are largely dependent on the UAS platform. For example, a quadrotor platform has the capability to hover over required areas and capture still images. On the other side, aerial videos from a fixed wing UAS, require further processing such as sensor data interpolation, image extraction, and flight line selection which is presented in detail in Sec.3. Different

application scenarios may require different types of remote sensing payloads including RGB cameras, NIR/thermal cameras, hyperspectral spectrometer, LIDAR, or RADAR. LIDAR (Light Detection and Ranging) has been widely used to generate 3-D digital representations of surfaces, and to calculate distances between points by measuring the lag between transmitted and reflected laser beams [9]. Radio wave based sensors such as synthetic aperture radars (SAR), an advanced form of side-looking airborne radars (SLAR) are used to create two or three-dimensional images of objects, such as landscapes, by using the motion of the RADAR antenna over target regions to provide fine spatial resolutions [10]. For the purpose of vegetation detection, rescue operation, surveillance, etc., multispectral and hyperspectral optical cameras are used onboard to acquire still images or videos.

Some of the most popular fixed wing remote sensing platforms and their respective sensing payloads are described below:

- Lancaster 5 [11]: Developed by PrecisionHawk [12] , the Lancaster 5 is a light weighted (5.3 lbs.) fixed wing UAS platform with a wingspan of 4.9 ft. Propelled by a single electric motor, this aircraft can carry payloads up to 2.2 lbs. It is equipped with LIDAR, visible, thermal/infrared sensors and a new 5-channel multispectral camera. It can achieve a flight time of 45 min and can cover 300 acres, which is advantageous for any agricultural mission. The Lancaster 5 is perfectly suited for applications across multiple industries including agriculture, energy & mining, insurance and energy response, and environmental monitoring.

- Minion 2.0 [13]: The current platform of AggieAir [14], Minion 2.0 is an electric powered fixed wing aircraft built specifically for aerial remote sensing independent of runways. It has a maximum take-off weight of 18 lbs. with payload capabilities of up to 4.5 lbs. The

Minion 2.0 can fly for 60 min at speeds up to 50 mph. AggieAir's current multispectral payload include 12 MP scientific grade RGB and grayscale cameras which can be modified by adding filters to produce required spectral data. The aircraft can also be equipped with a 640×480 thermal infrared camera and optional SWIR camera. This sensing payload is capable of capturing time-synchronized images at 1.5 FPS with 1TB onboard storage for possible mission times of over 3 hours.

- UX5 [15]: UX5 is a fixed wing UAS platform developed by Trimble [16]. It has a total weight (including payload) of 2.5 kg with a wingspan of 1m. Manufactured using Expanded Polypropylene (EPP) foam with carbon frame structure and composite elements, the UX5 has an endurance of up to 50 min at cruise speeds of up to 80 km/h. With a flying range of 60 km and ceiling up to 5000m, this platform is highly suitable for vegetation monitoring, topographic surveying, infrastructure inspection, etc. For the purpose of multispectral imaging, this platform can be equipped with a 5-band MicaSense RedEdge narrowband camera. This camera collects 5 bands, namely, red, blue, green, rededge and near infrared into distorting free 12-bit uncompressed TIFF files, resulting in a radiometric data quality comparable to satellite systems.

- The Tempest [17]: The Tempest was designed by UASUSA [18] for University of Colorado, for National Science Foundation (NSF) Tornado research project, Vortex2. It is a fixed wing platform with a wingspan of 10 ft. It weighs 10 lbs. with payload capabilities of over 7 lbs. It has an endurance of over 1.5 hours at wind speeds of 60 mph which makes it suitable for applications such as emergency response, agriculture surveying, mapping, etc. The Tempest can be equipped with any customized sensing payloads including infrared (IR) cameras and daytime stabilized cameras.

The following sections focus on some of the important contributions of researchers in the fields of UAS based remote sensing and photogrammetry.

1.2.5 UAS Multispectral Remote Sensing Applications

Researchers in the past have used optical cameras including RGB and NIR cameras on UASs for different multispectral remote sensing applications. The application of the NDVI for the use of precision agriculture using the visible and near-infra red spectrums is shown by Rua *et.al* [19]. "AggieAir' multispectral imagery was used for agriculture applications including, estimation of evapotranspiration rates, crop tissue nitrogen and chlorophyll, surface and root-zone soil moisture, and crop leaf canopy volume. Band re-configurable multi UAS- based remote sensing can be used for real time water management and distributed irrigation control [20]. An overall investigation on the issues and considerations of applying conventional vegetation indices to UAS derived orthomosaics is provided by Klaas Pauly [21].

Multispectral and hyperspectral optical cameras require an accurate radiometric and reflectance calibration to guarantee good results. The effect of bi-directional reflectance distribution function on remote sensing imagery from small UASs is explored by Stark *et.al* [22], where, the effects of wide field of view (FOV) of imaging sensors and solar motion on UAS based remote sensing are analyzed. Zaman *et.al* [23] developed a semi-automatic model to calculate the reflectance factors of red, green and NIR bands with the help of white Barium Sulfate ($BaSo_4$) panel and a Halon board. This method considers the effects of the sun zenith angle on the reflectance properties of objects.

1.2.6 Other Application Scenarios

The use of UASs for fire monitoring has become popular over the years. Small UAS is a feasible option for such applications because they are low cost, easy to handle, and have high

spatial and temporal resolutions. However, there exist many challenges to employ small UASs for the monitoring of prescribed fires or wildfires including high temperature, strong turbulence, and fast fire dynamics. Most important of all, the flight performance of small UASs in such high thermal and unstable atmospheric conditions need to be analyzed first in order to achieve safe and efficient monitoring of prescribed or wild fires. Casbeer *et.al* [24] developed an effective path planning algorithm using infrared images which are procured from the on-board camera for forest fire boundary following. The use of multiple cooperative Low-altitude short endurance (LASE) UASs for fire monitoring has been investigated by Sujit *et.al* [25], by using service agent UASs and detection agent UASs (fire detection and communication with service agent UASs). Ononye *et.al* [26], utilized the Dynamic Data Acquisition system to determine fire perimeter, fire line and fire propagation direction with the help of multispectral aerial imagery.

Images from UASs can also be used to extract digital elevation models (DEMs) which can be used to measure the surface elevation. Birdal *et al* [27] were able to estimate the tree height with a correlation of 94 % with ground measurements and root mean square (RMS) error of 28 cm.

Since UASs generally use low-cost sensors, it is important to perform calibrations in order to increase their robustness. Aerial imagery can be used to perform the calibration of the onboard inertial sensors with the use of ground control points (GCPs), as shown by Jensen *et.al* [28]. An error range 5-45m for the GCPs before calibration and 5-20 m after calibration was observed by them.

1.3 Contribution and Organization

The major contributions of this thesis include:

- An efficient procedure for generation of multispectral aerial maps (RGB, NIR, and CIR) using aerial videos or images from KHawk UASs.

- A robust NDVI calibration procedure using ground targets with known reflectance values.

- A comprehensive error analysis for the generated aerial maps.

The organization of this thesis is described as follows. Chapter 2 focuses on the general requirements for unmanned remote sensing platforms and introduces the two unmanned aircraft systems (UASs) used in this thesis. Chapter 3 provides detailed descriptions of the image geotagging procedure and consequent photogrammetric processing for aerial map generation followed by a comprehensive error analysis for validation. Chapter 4 introduces our method for the multispectral aerial map generation and NDVI calculation. Chapter 5 focuses on the implementation of multispectral remote sensing in two applications, namely, prescribed fire monitoring and tree height estimation. Chapter 6 provides the final conclusions of the contributions presented in this thesis and suggests future recommendations.

2 KHawk UAS

2.1 Introduction

The weight, size, and onboard avionics of a UAS have a big impact on the success of any surveillance and reconnaissance mission. This chapter focuses on the general requirements for unmanned remote sensing platforms and detailed descriptions of the two unmanned aircraft systems (UASs) used in this thesis, a KHawk 48" UAS and a KHawk 55" UAS. Both KHawk UASs were designed and built by researchers at the Cooperative Unmanned Systems Laboratory (CUSL) in the University of Kansas (KU).

2.2 Remote Sensing Requirements

Remote sensing is defined as the analysis of the Earth's surface without making physical contact with it [29]. There are many civilian and military applications of remote sensing, including search and rescue, vegetation surveying, herd monitoring, terrain structure mapping, soil status measurement, etc.

In recent years, the use of UASs as remote sensing platforms have become popular due to their advantages such as low cost, easy handling qualities, and high spatial/temporal resolutions. The development of an effective unmanned remote sensing platform depends on certain specific requirements such as:

- Short preflight preparation time: For emergency operations such as search and rescue, disaster evaluation, wildfire monitoring, it is important to be able to take off and fly to the areas of interest quickly.

- Easy to launch: The ability of a platform to be launched, independent of the terrain, is essential for survey missions over different types of surfaces such as crop fields, mountains or water areas.

- High endurance: A good remote sensing platform should have high endurance in order to cover agricultural or environmental fields, which are generally large scale (several square miles or bigger). Since most UASs fly at lower altitudes ($<$ 400 ft.) and cover smaller areas, compared with manned aircraft or satellites, they might be required to fly long durations.

- High performance in waypoint tracking: In order to construct high-quality aerial maps, it is imperative that the UAS platform adheres to its pre-programmed flight plan and not deviate to a large extent while maintaining a good cruise speed. The platform should also perform robustly in challenging weather conditions such as strong winds and turbulence.

- Communication Range: Vegetation survey may require a large area coverage in order to analyze the spatial patterns of canopies. It is essential that the unmanned remote sensing platform has a long communication range with the ground station while flying autonomously.

- Weight, size, and placement: The placement of the imaging payload on the UAS is extremely crucial for the generation of high-quality aerial imagery, especially for fixed wing platforms. Nadir facing aerial imagery can greatly simplify the image georeferencing procedure.

- Multi-payload capability: The UAS platform must meet the weight and size requirements for single or multiple payloads. Multispectral or hyperspectral remote sensing sometimes require two or more instruments onboard, for example, RGB and NIR cameras.

- Sensor synchronization: Easy payload triggering and GPS/INS/image synchronization can simplify the orthorectification process.

Two KHawk UAS platforms are introduced in detail in the next two sections following the above requirements.

2.3 KHawk Flying Wing – 48" UAS

KHawk 48" UAS is a flying wing aircraft made from a Unicorn wing with a wingspan of 48". The aircraft is powered by a pusher-type propeller and an electric brushless motor. It has two elevons as the control surfaces for roll and pitch control, shown in Figure 1.
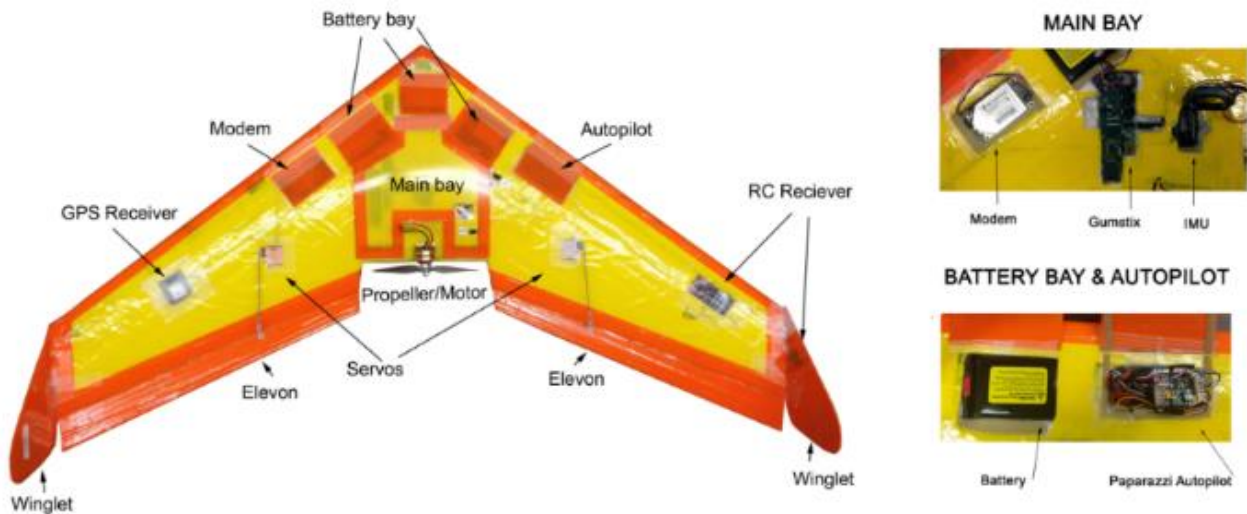
Figure 1. KHawk 48 UAS description.

The airborne system of KHawk 48" UAS includes inertial sensors (Micro strain GX2 IMU and u-blox 5 GPS receiver), actuators (elevon and throttle motor), a data modem, a Gumstix computer, an open source Paparazzi autopilot and lithium polymer batteries. The aircraft supports both manual RC mode and autonomous mode. A PeauPro82 GoPro Hero 4 camera is installed for aerial video acquisition. All the sensor data is logged onboard the aircraft including inertial data (100 Hz) and GPS data (4 Hz).

KHawk 48" UAS satisfies most of the requirements described in the previous section. It can be launched using a bungee, which is independent of runway to support operations over different types of terrain. In addition, KHawk 48" UAS has a short preflight preparation time of about 5 minutes with launch ready status. It has a flight endurance of about 30 minutes and can

fly as far as 2 km away from GCS with a 3 dB ground antenna. KHawk 48" UAS supports payload up to 1.5 lbs.

2.4 KHawk Flying Wing – 55" UAS.

KHawk 55" UAS (Figure 2) is a flying wing aircraft made from EPOR foam with a wingspan of 55". It is equipped with similar avionics with KHawk 48", which can support autonomous GPS waypoint tracking as well. Six 11.1V 2000 mAh batteries are used to power, which can support up to 45 minutes of flight with the minimal takeoff weight. A PeauPro82 GoPro Hero 4 camera and a pitot-tube system (dynamic pressure) were installed for data collection. All the sensor data is logged onboard the aircraft including inertial data (100 Hz), GPS data (4 Hz), and airspeed data (50 Hz).

Figure 2: KHawk 55 UAS description.

Similar to KHawk 48" UAS, KHawk 55" UAS also has a short preflight preparation time of about 5 minutes with launch ready status. It has a flight endurance of about 45 minutes. It can support payload weighing equal or less than two pounds. Both KHawk UASs are built to sustain adverse weather conditions, such as high winds (<12 mph) and turbulence. The major drawback of these platforms is their incapability to carry multiple cameras at the same time.

2.5 Imaging Payload

Two PeauPro82 GoPro Hero 4 Black Cameras (Figure 3) are used for aerial video acquisition onboard KHawk UAS 48" and KHawk UAS 55". The fisheye lens is replaced with a 3.97mm lens with minimal radial distortions for one and 3.37 mm lens with RED+NIR (NDVI) filter for the other. The camera specifications are shown in Table 1 .

Figure 3. PeauPro82 GoPro Hero 4 Black.

Table 1. Specifications for PeauPro82 GoPro Hero4 RGB/NDVI camera [30].

Description	Value
Weight (g)	90
Dimensions (Diameter x Length) (mm)	17.40×22.48 mm
Update frequency (Hz)	23.97 , 29.97
Resolution Mode (p)	1920×1080

3 KHawk Aerial Map Generation

3.1 Introduction

This chapter provides detailed descriptions of the image geotagging procedure and consequent photogrammetric processing for aerial map generation using KHawk UASs. The proposed procedure can support both digital images and videos, which is ideal for monitoring of fast evolving processes such as wildfires.

Image geotagging is the process of assigning corresponding location and orientation information to each aerial image, based on onboard GPS and inertial telemetry. This process is highly dependent on the UAS type. For instance, a quadrotor can hover over selected regions and take still images. On the other side, aerial videos from a fixed wing UAS, require further processing such as sensor data interpolation, image extraction, and flight line selection.

Photogrammetry is defined as the technique to measure the 3D coordinates using photographs as a medium for metrology. The fundamental property of photogrammetry is to produce 3D models or maps of a real world scene from multiple individual images [31, 32]. These maps could be further used for many applications, such as surface elevation determination from DEMs, estimation of vegetation patterns, and detection of crop canopy using NDVI. A complete description of the mapping procedure and necessary parameters required to achieve a high-quality 3D model is provided in the later parts of this chapter.

Sec. 3.2 and 3.3 focus on preflight procedures such as camera calibration and flight path generation. Sec. 3.4 and 3.5 describe the image geotagging procedure. Sec. 3.6 provides detailed descriptions of the photogrammetric processing using Agisoft Photoscan software. Lastly, a comprehensive error analysis is presented in Sec. 3.7, which validates the entire aerial map generation procedure.

3.2 Camera Calibration

Camera Calibration is the process of estimating the parameters of a camera using special calibration images [33]. Camera parameters can be categorized into intrinsic and extrinsic ones. The intrinsic parameters include the focal lengths, optical center, and skew coefficient. These are internal to the camera. These parameters play an integral role in mapping between 3D coordinates in the camera body frame and the 2D pixel coordinates in the image frame. The focal length of the camera enables the calculation of the Field of View, and therefore the footprint coverage area at different altitudes. The intrinsic camera parameters are determined using the equations shown below:

$$x_{pix} = \frac{u'}{w'}, y_{pix} = \frac{v'}{w'}, \tag{1}$$

$$\begin{bmatrix} u' \\ v' \\ w' \end{bmatrix} = \begin{bmatrix} \alpha_x & s & x_0 & 0 \\ 0 & \alpha_y & y_0 & 0 \\ 0 & 0 & 1 & 0 \end{bmatrix} \begin{bmatrix} x_s \\ y_s \\ z_s \\ 1 \end{bmatrix}, \tag{2}$$

where $\alpha_x = fk_x$, $\alpha_y = -fk_y$ and x_s, y_s, and z_s are object world coordinates.

The extrinsic parameters define the location and orientation of the camera with respect to the world frame. Images of a chess board are collected to perform the calibration of the PeauPro82 GoPro Hero 4 RGB camera used on KHawk UASs. Figure 4 represents the extrinsic parameter visualization of the PeauPro82 GoPro Hero 4 camera.
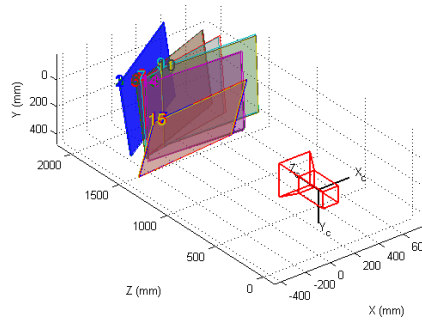
Figure 4. Extrinsic parameter visualization.

15

The focal lengths of PeauPro82 GoPro Hero 4 RGB camera are estimated to be 1651.4 pixels and 1666.6 pixels in the horizontal and vertical directions respectively, which are further used to calculate the fields of view. In order to estimate the accuracy of the calibration, reprojection errors are calculated. Reprojection error is defined as the geometric error corresponding to the image distance between a projected point and a measured one [34]. Figure 5 represents the mean reprojection error in pixels per image. An error of 0.45 pix is achieved.
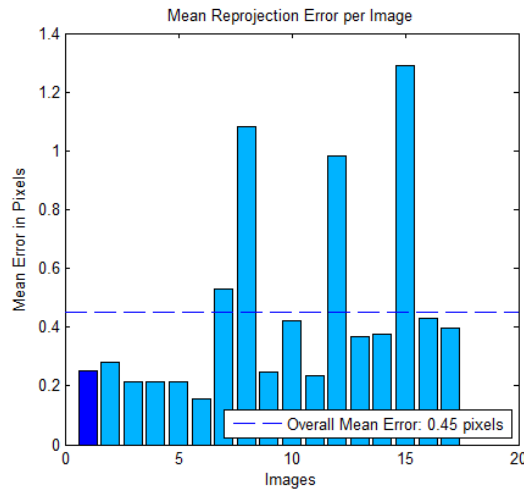
Figure 5. Mean reprojection error per image.

3.3 Flight Plan Generation.

The selection of the UAS flight plan is critical to the success of any UAS based remote sensing mission. Characteristics such as pixel resolution, cruise speed, flight altitude and flight line pattern play an integral role in determining the feasibility and robustness of a remote sensing operation. In order to generate a good flight plan, certain factors such as mission objectives, UAS and camera capabilities and weather conditions need to be considered. A typical flight plan generation problem is presented and described.

Let r be the optimal pixel resolution required to satisfy the specific remote sensing objective. For example, 0.1 meter per pixel. Given the camera properties such as image pixel

resolution $P_h \times P_v$, focal length f, the fields of view θ_h, θ_v and the camera footprint coverage area $FP_h \times FP_v$ (Figure 6) can be calculated. The camera is installed downward-looking with its horizontal axis parallel to the aircraft y-axis.
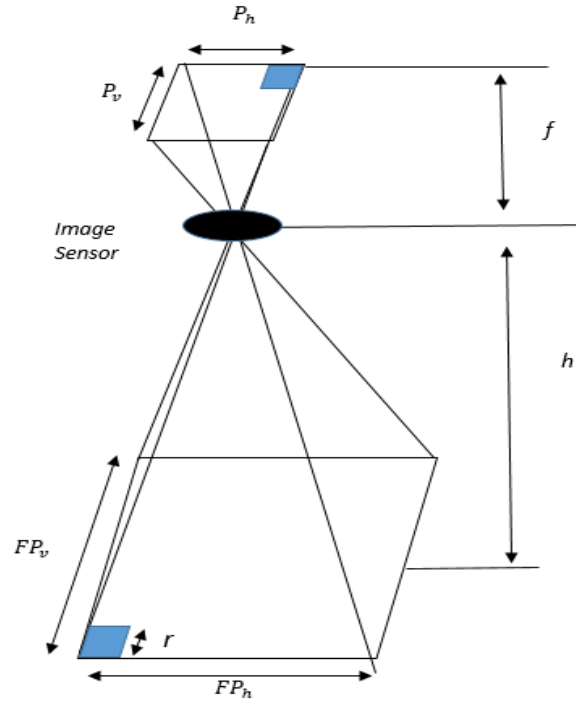
Figure 6. Footprint area calculation.

$$\theta_h = 2\tan^{-1}\frac{P_h}{2f}, \quad \theta_v = 2\tan^{-1}\frac{P_v}{2f}, \tag{3}$$

$$FP_h = h\frac{P_h}{f}, \; FP_v = h\frac{P_v}{f}. \tag{4}$$

The desired flight altitude h can be determined as follows:

$$h = fr \tag{5}$$

The maximum overlapping distance between each flight line $D_{FL,max}$ can be determined, using the desired flight altitude h, fields of view θ_h, θ_v and minimum lateral overlapping percentage σ required for image stitching.

$$D_{FL,max} = \sigma h\frac{P_h}{f} \tag{6}$$

It is worth mentioning that the UAS autopilot needs to be flexible enough to support real time adjustment of flight trajectories based on tracking performance. Figure 7 shows a typical flight plan with minimal image overlapping percentage over the area of interest. Each colored rectangle represents the camera footprint at each time step and the lines represent the UAS flight plan. After the completion of the flight, data is collected and processed to facilitate the aerial map generation, which is described in the following sections.
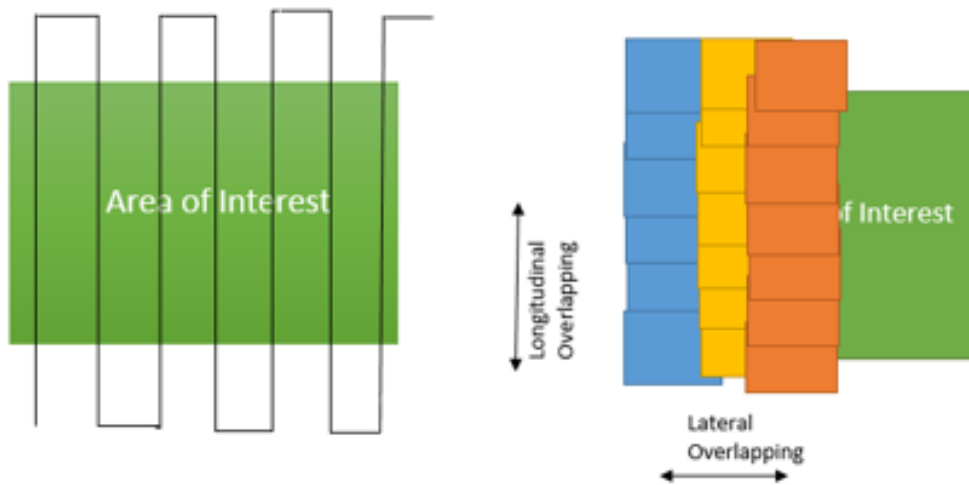
Figure 7. UAS flight plan with image overlay.

3.4 Sensor Data Synchronization

Once all the flight data is collected, the next step is to synchronize the GPS, IMU and vision data. In this case, the synchronization is performed with respect to the camera frequency for further processing. The take-off time is selected as the pivotal point for synchronization, which is estimated via visual inspection of the video. Given the aircraft ground speed V, and altitude h from GPS, x-acceleration a_x from IMU, the take off time corresponding each of these sensors can be selected based on:

$$V > 18 \text{ m/s}, \quad h > h_g, \tag{7}$$

$$a_x > 2G, \tag{8}$$

where h_g is ground altitude.

Figure 8 and Figure 9 show the altitude and x- acceleration data respectively. Once the GPS and IMU take off time is determined, a simple linear interpolation is performed in MATLAB for the synchronization.
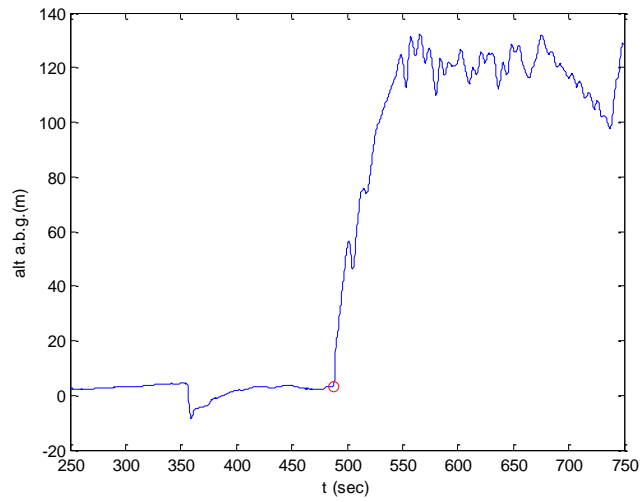
Figure 8. Altitude vs time for GPS take off time selection.
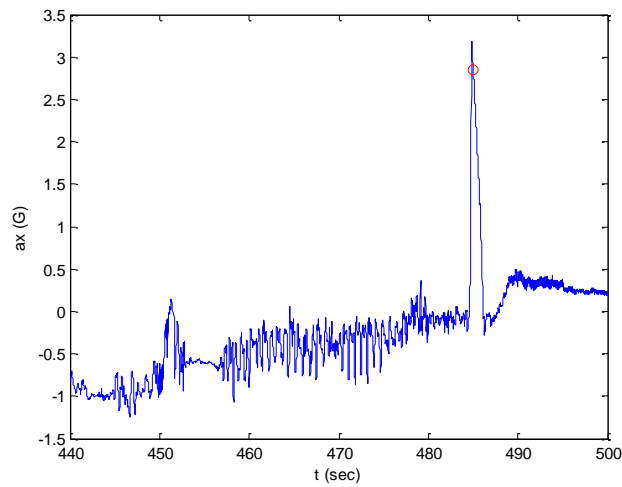
Figure 9. Acceleration (x-direction) vs time for IMU take off time selection.

19

3.5 Image Selection

After the sensor synchronization, the next step is to select necessary images for the mapping. The selection of images is based on two major factors:

- Area of interest: The selected images need to cover the required area of interest;

- Aircraft attitude: In order to obtain a high-quality map, a minimal overlapping percentage is required between images. To ensure this, it is recommended to select images taken during straight and stable flight lines.

After all the images required for the map generation are selected, they are extracted from the aerial video and imported into Agisoft Photoscan software for the photogrammetric processing, which is described in detail in the next section.

3.6 Photogrammetric Processing.

Photogrammetry is the science of using photographs as a medium for measurement. This is the final part of the aerial map generation process, where the geotagged images are combined with overlapping fields of view to produce a high-quality map. Agisoft Photoscan Pro software is used for the map generation.

Agisoft Photoscan Pro is a stand-alone software that performs photogrammetric processing of digital images and generates 3D spatial data [36]. It is widely used in different aerial image processing scenarios for both research and industrial applications. The pro edition of the software is equipped with the following functionalities:

- Georeferencing: the process of associating an aerial image or map with its geographical coordinates;

- DEM export in GeoTIFF elevation data, Arc/Inpho ASCII grid, band interleaved file format, XYZ file formats;

- Orthophoto generation: the process of geometrically correcting an aerial image to ensure uniform scale;

- Carrying out area and volume measurements;

- Python scripting.

A general work flow is presented for the entire process in this section.

3.6.1 Image Management

The selected images are imported to the software in PNG format along with their respective location and orientation information. The software automatically matches the images with their coordinates and places them accordingly as shown in Figure 10. The blue lines represent the flight path of the aircraft corresponding to the images' location and orientation.
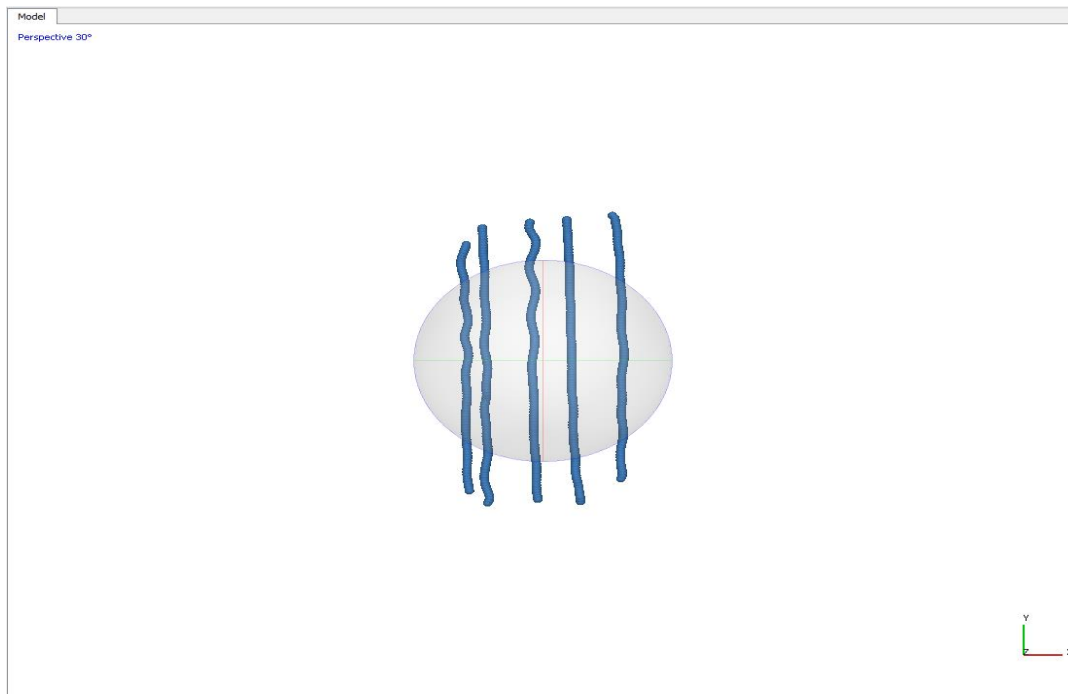
Figure 10. Image management.

3.6.2 Image Alignment

The next step is the image alignment. Agisoft performs the alignment based on feature matching between consecutive images. The alignment specifications are specified as shown in Figure 11.
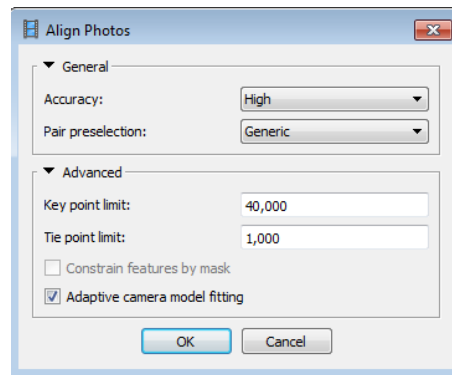
Figure 11. Image alignment specifications.

A brief definition of each of the specification is provided.

- Accuracy – Agisoft determines the accuracy of the alignment process. **High** was chosen, keeping quality as well as computational costs in mind.

- Pair Pre-selection - Agisoft provides an option wherein the photos are pre-paired before the actual alignment. **Generic** was chosen since the images are tagged with position and orientation information. The software first makes the pair selection based on the GPS data, before performing feature matching. This can speed up the alignment process.

- Key Point Limit – This parameter specifies the number of points Agisoft will extract per image. A value of **40,000** was chosen based on recommendations made by experts.

- Tie Point Limit – Number of points chosen for final alignment process. A value of **2000** was chosen, which means that out of the 40,000 points Agisoft picks, the best 2000 is used for image alignment.

The resulting alignment is shown in Figure 12.

Figure 12. Image alignment.

3.6.3 Dense Cloud Construction

After the images are aligned, the next step is to build a dense cloud, which in turn facilitates the building of DTM and DEM. Based on the estimated image positions, the software calculates the depth information for each image. The specifications used to perform this function are shown in Figure 13.
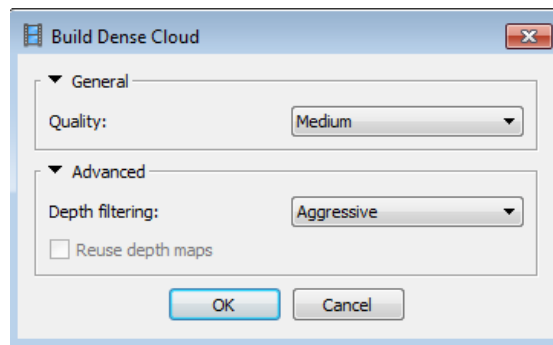
Figure 13: Dense cloud construction specifications.

A brief definition of each of the specification is provided.

- Quality – Determines the quality of dense cloud construction. **Medium** was chosen, in order to reduce computational time.

- Depth Filtering – Filters out certain points that are far from the defined area. **Aggressive,** being the default option was chosen.

Figure 14 shows the final dense cloud.
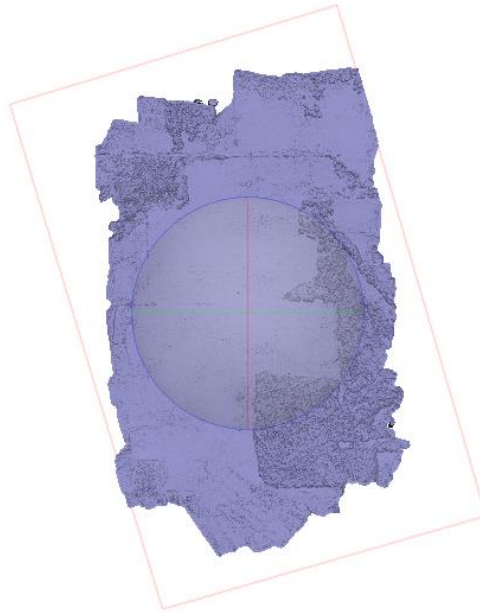
Figure 14. Dense cloud.

3.6.4 Mesh Construction

Mesh construction or 3-D model construction is the process of building a 3-D polygonal model. The quality of the model depends entirely on the dense cloud, as shown in Figure 14. The specifications used to perform this function are shown in Figure 15.
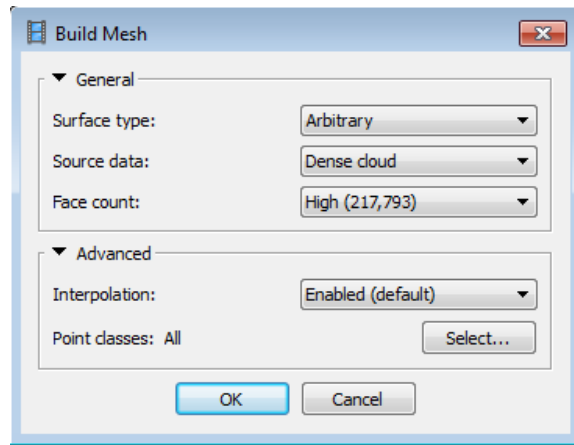
Figure 15. Mesh construction specifications.

The final 3-D model can be observed in Figure 16.

Figure 16. Mesh construction-3D model.

3.6.5 Dense Surface Reconstruction

DEM generation, one of the key tasks for any photogrammetry software, takes only minutes in Agisoft, due to the sophisticated image matching and autocorrelation algorithms. Figure 17 shows the DEM for the corresponding aerial map.
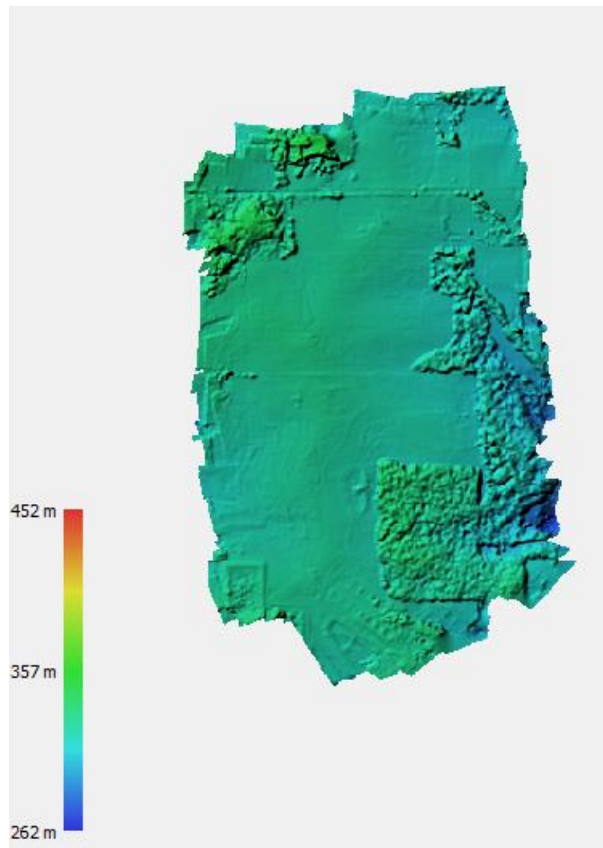
Figure 17. Digital elevation model.

3.6.6 Orthophoto Generation

After creating a 3D model of the area with Agisoft, orthorectification can be performed. The final orthorectified maps may be exported from the software as a TIFF, PNG or JPEG image file, and as a KMZ file, which can be imported into GIS software for geographical validation [37]. Figure 18 and Figure 19 represent the final aerial maps with necessary details such as scale bar, resolution, north arrow.

KU Field Station
June 7.2017
Pixel Resolution: 0.10m
RGB Map

0 25 50   100   150   200
                              Meters
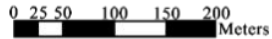
Figure 18. Final aerial map.

Figure 19. Final aerial map overlaid on Google Earth.

A survey data image (Figure 20) can also be extracted, which provides information on the camera locations and image overlay percentage. Blue indicates highest image overlay percentage and red indicates the least. Other specifications of the map are listed in Table 2.

Table 2. Aerial map specifications.

Description	Value
Number of images	499
Pixel resolution (m/ pix)	0.10
Coverage area (km^2)	0.886
Location 2D error (m)	17.72
Total computational time	1 hour 28 min

27
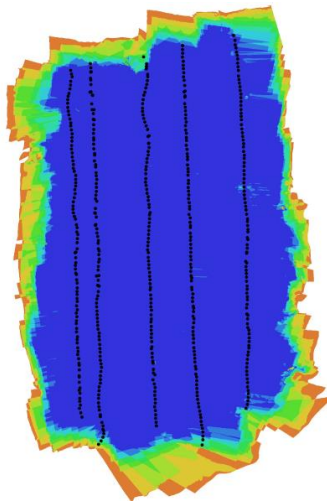
Figure 20. Camera locations and image overlay percentage of aerial map.

As observed in the above table, a location error of 17.72 m is estimated from the map generating procedure. However, a more comprehensive error analysis is performed using ground control points (GCPs) to validate the accuracy of the image georeferencing and stitching procedure which is presented in the next section.

3.7 Error Analysis

A comprehensive error analysis using ground control points was performed to quantify the accuracy of the aerial maps. The coordinates of ground control points from the generated aerial map were compared with ground GPS (Ublox and NovAtel) measurements. In order to enhance the robustness of the method, Real Time Kinematic technique (RTK) using RTKLIB software was used to improve the ground GPS accuracy. Two flight tests were conducted for this analysis.

A flight test was conducted on the 26th of May, 2017 at the KU field station. A KHawk 48" UAS was equipped with a PeauPro82 GoPro Hero 4 black RGB camera. Four target boards (1m × 0.7 m) were used as the ground control points (Figure 21) and were placed near the ground

station. They were placed in the shape of a quadrilateral with an approximate distance of 30 m between them. A NovAtel GPS receiver and an Ublox GPS unit were placed at each point for about three minutes for ground data collection.

Figure 21. Aerial view of GCPs.

The collected GPS coordinates are converted into Universal Transverse Mercator (UTM) coordinates, shown in Figure 22. The distribution of the GCP coordinates from ground GPS including Ublox, NovAtel raw and NovAtel RTK are compared with the vision estimates, shown in Figure 22- Figure 25.
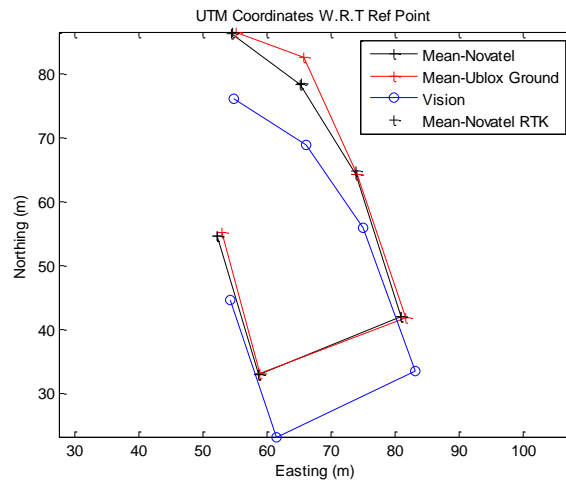
Figure 22. UTM coordinates of GCPs.
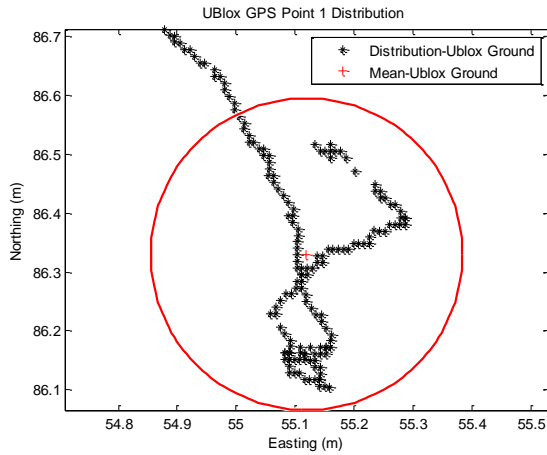
Figure 23. Ublox GPS distribution.
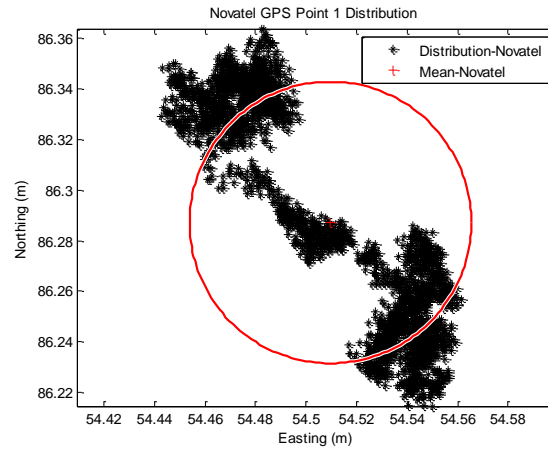
Figure 24. NovAtel GPS distribution.
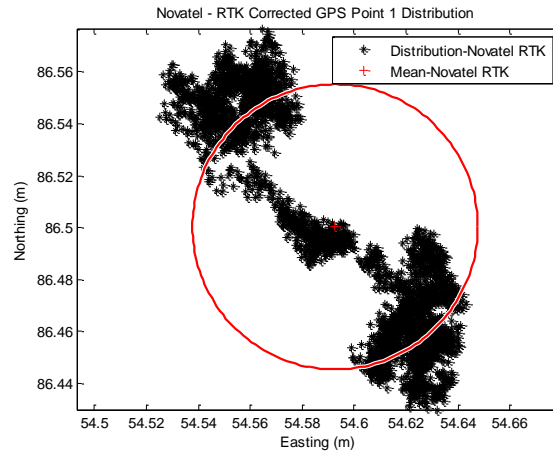
Figure 25. NovAtel-RTK GPS distribution.

Table 3 represents the mean, maximum and minimum 2-D errors between the GPS coordinates obtained from the aerial maps and the ground receivers. It also presents the standard deviation of the Ublox, NovAtel and RTK corrected NovAtel GPS receivers from the distribution characteristics shown in Figure 22- Figure 25. It should be noted that the Ublox and NovAtel GPS are claimed to have a horizontal accuracy of 2.5m and 1.5m respectively.

The second flight test was conducted on the 7th of June, 2017 at the KU field station. Two landmarks (a weather station and a power pole), two cars and the tent were used as the GCPs (Figure 26). A NovAtel GPS placed on each point for ~ 3 minutes for data collection.

30

Table 3 Errors and standard deviations, GCP flight test I.

Description	Ublox	NovAtel	NovAtel-RTK Corrected	Agisoft
Minimum error (m)	8.42	8.325	8.847	-
Mean error (m)	10.27	9.5	9.67	17.72
Maximum error (m)	13.83	10.18	10.39	-
Standard deviation (m)	0.088	0.01856	0.01830	-

Figure 26. Aerial view of GCPs.

Table 4 represents the mean, maximum and minimum errors between the GPS coordinates obtained from the orthorectified maps and the ground receiver. It also presents the standard deviation of the NovAtel and RTK corrected NovAtel GPS receivers.

Table 4. Errors and standard deviations, GCP flight test II.

Description	NovAtel	NovAtel-RTK Corrected	Agisoft
Minimum error (m)	4.90	4.94	-
Mean error (m)	7.73	7.72	13.6
Maximum error (m)	9.80	9.83	-
Standard deviation (m)	0.0256	0.0248	-

It can be observed in both cases that Agisoft over-predicts the location error. In addition, RTK correction does not seem to improve the accuracy of the NovAtel ground GPS receiver. This

could be due to the fact that the closest base station (ksul at Manhattan, KS) is 80 miles away from the rover receiver. However, further test needs to be conducted for a complete analysis. The two aerial maps shown in this chapter have a coverage area of $0.557/0.828\ km^2$ and pixel resolutions of ~ 0.10 m with a mean distance errors of ~ 10/7.5 m.

3.8 Chapter Summary

In this chapter, the KHawk aerial mapping procedure is proposed. An optimal flight plan generation procedure for specific remote sensing applications is presented. A thorough explanation of the image geotagging and photogrammetric processing for KHawk UAS platforms is provided. Finally, a comprehensive error analysis is conducted to validate the aerial map generation procedure. For the current system, KHawk UAS can generate aerial maps with a coverage area of 5 km×5 km with an accuracy of less than 10 m. The KHawk 48" UAS can achieve a pixel resolution of 0.10 - 0.12 m at a flying altitude of 120 m using PeauPro82 GoPro Hero 4 cameras (RGB/NIR).

4 Multispectral Remote Sensing

4.1 Introduction

The purpose of this chapter is to introduce our method for multispectral aerial map generation and NDVI calculation. As mentioned in Sec.1.2.2, multispectral based vegetation indices such as NDVI, SAVI and EVI can be used for applications including vegetation detection, crop analysis, moisture estimation and soil status analysis. The work presented in this thesis utilizes NDVI to perform vegetation survey and analysis, which is discussed in further details in the later parts of this chapter.

Sec. 4.2 provides a detailed description of the KHawk multispectral aerial mapping and a brief introduction to NDVI. Sec.4.3 focuses on the proposed NDVI calibration methods, followed by a comprehensive ground test procedure and its respective results. Finally, the calibration procedure is implemented on real flight test data for further validation.

4.2 Multispectral Aerial Mapping

KHawk UASs can be used to generate raw multispectral aerial maps as well as processed maps such as CIR map or NDVI map. The generation of multispectral map is similar to the RGB map introduced in Chapter 3. The main difference lies in the normalization of pixel digital numbers to their respective reflectance values. The KHawk 48" UAS is equipped with a PeauPro82 GoPro Hero 4 NDVI camera. The multispectral imagery obtained from the NDVI camera is used to generate NIR and red band spectral maps, as shown in Figure 27 and Figure 28. An interesting observation can be made from these maps in terms of the reflectance properties of vegetation. Trees and other vegetation appear brighter in Figure 27 than in Figure 28 This is due to the fact that, the vegetation reflects more NIR band than red band.

The red and NIR spectral maps generated are used to construct a color infrared (CIR) map (Figure 29). Applications of CIR maps include plant species identification, vegetation biomass estimation, tornado damage tracking, soil moisture assessment and turbidity assessment [38].

Figure 27. NIR map.

Figure 28. Red map.

Figure 29. CIR map.

A summary of the different color representation in the CIR map is shown in Table 5.

Table 5. CIR map color representation.

Color	Description
Red and lower tones of red	Dense vegetation (trees)
Pink and Magenta	Medium vegetation (Short grass, shrubs)
White and light blue.	Low vegetation (Soil, concrete, gravel)
Dark Blue	Water, high moisture

NDVI or the normalized difference vegetation index is a graphical indicator, which can be used for remote sensing measurements, mainly in fields of agriculture, biology, and other geosciences. The NDVI of an object or area of interest is calculated based on the spectral reflectance values corresponding to the NIR and red bands as shown below:

$$NDVI = \frac{R_{NIR} - R_R}{R_{NIR} + R_R} \tag{9}$$

where, R_{NIR} and R_R represent the reflectance values of NIR and red band respectively.

The NDVI values typically range from -1 to 1 [39]. Areas of no vegetation, such as barren land, rock, sand, etc., show very low NDVI values (less than 0.1), areas of low and sparse vegetation, such as shrubs and short grass show values in the range of 0.2-0.5, and trees during their peak growth stage show the highest range (0.6-0.9), water shows negative NDVI values [39]. Figure 30 shows a sample NDVI calculation. It is worth mentioning the raw NIR/Red band images need to be calibrated for accurate NDVI calculation, which is introduced in detail in the following section.
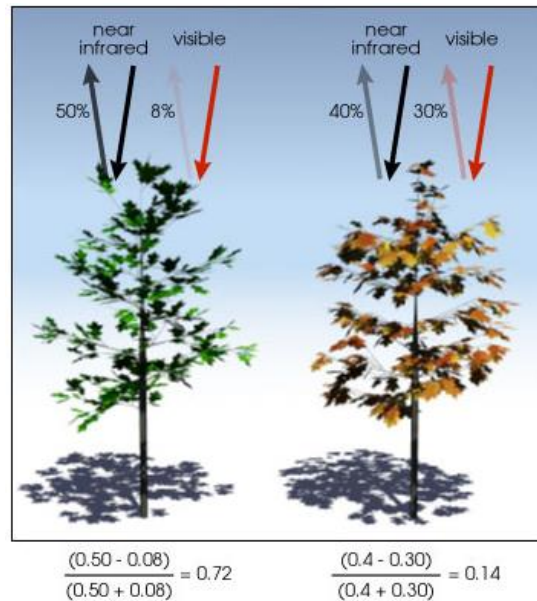

Figure 30.NDVI Calculation [40].

4.3 NDVI Calibration

The raw data of an image is represented as Digital Numbers or DNs. Each pixel has a number assigned to it, depending on the bands and light intensity. For example: an 8- bit NIR image will have a DN range of 256. NDVI cannot be calculated using only the raw DN since they are not calibrated and contain information such as light intensity, reflectance, atmospheric conditions and sensor characteristics. Accurate calibration is required in order to compensate for all the parameters using boards with known reflectance values. This section focuses on the calibration procedure developed using the MAPIR ground target reflectance board [40]. The calibration problem is defined below followed by an introduction to spectral reflectance in the next subsection.

NDVI Calibration Problem

Given a ground reflectance target board comprising of three Lambertian surfaces with known reflectance values R_1, R_2, R_3, and raw DNs I_1, I_2, I_3 from a multispectral image, a linear relationship can be obtained. The characteristics of the linear function (K and b) can be determined from the linear regression (10, 11). Then these parameters can be applied to any image for the conversion from raw DNs to reflectance for each band. The acquired reflectance values can be further used to calculate the NDVI for each pixel.

$$R_{NIR} = K_{NIR}I_{NIR} + b_{NIR} \tag{10}$$

$$R_{red} = K_{red}I_{red} + b_{red} \tag{11}$$

Note, certain factors such as NIR noise and Gamma re-correction need to be considered for accurate calibration, which are explained in further details in the following sections. A comprehensive description of an NDVI calibration ground test is presented in Sec.4.3.3.

4.3.1 Spectral Reflectance

The reflectance of a material is its effectiveness in reflecting the radiant energy. It is the fraction of the electromagnetic power that is reflected at the interface. Spectral reflectance curve is the plot of the reflectance as a function of wavelength as shown in Figure 31. Note that the NIR reflectance value of water is zero, which explains why it has a negative NDVI value.
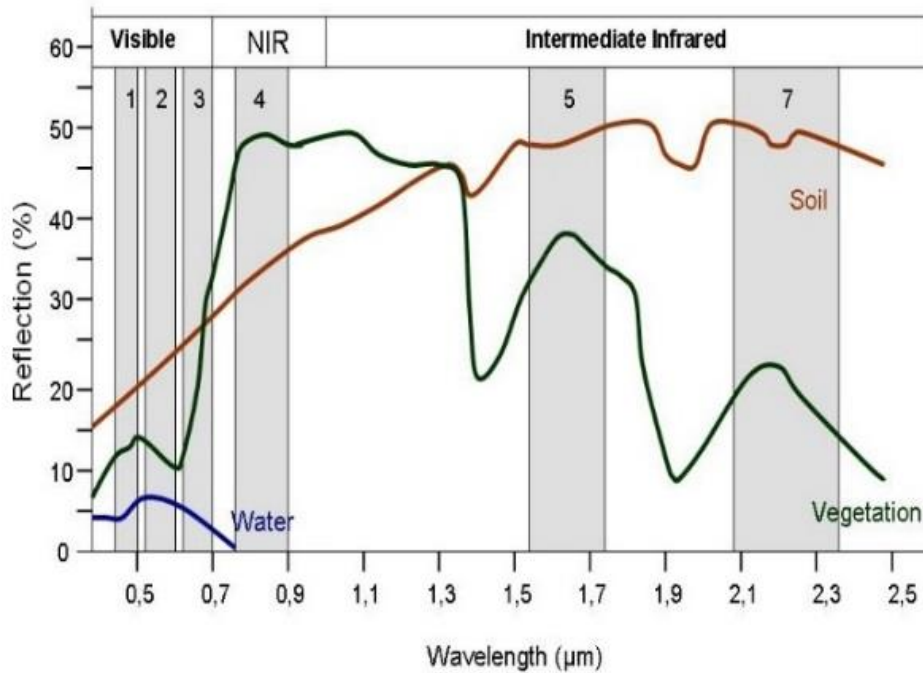
Figure 31. Spectral reflectance curve [42].

Reflectance Calibration is a procedure which is used to formulate the relationship between the raw DN and the reflectance value for each pixel. These reflectance values are then used to calculate the NDVI and other important vegetation indices. To perform this calibration, boards with known reflectance values are required. The MAPIR calibration ground target (Figure 32) was used for the calibration. The board is comprised of Lambertian surfaces with known spectral reflectance curves (Figure 33).

Figure 32. MAPIR reflectance ground target board [41].
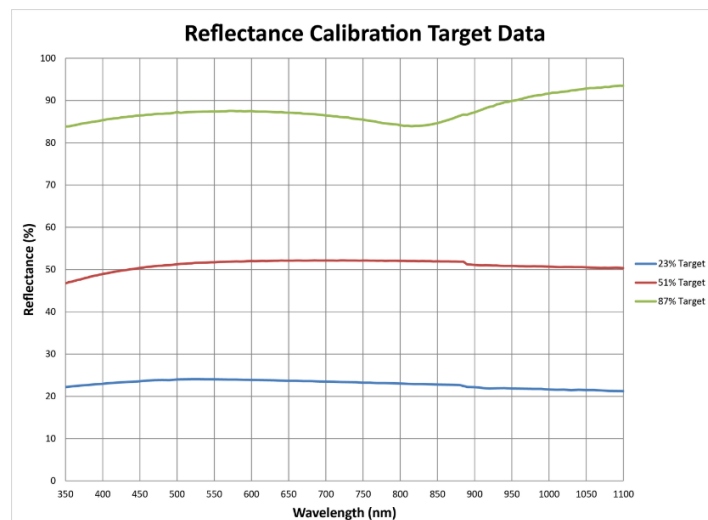
Figure 33. MAPIR board spectral reflectance curve [41]

The reflectance values for wavelengths corresponding to 660nm and 850nm (red and NIR respectively) for each of the Lambertian surface on the MAPIR target board was logged as ground truth as shown in Table 6.

Table 6. Reflectance values of MAPIR target board.

Bands	Surface 1 (%)	Surface 2 (%)	Surface 3 (%)
Red (660 nm)	87.3	52.13	23.66
NIR (850 nm)	84.30	51.95	22.69

4.3.2 Factors Influencing Calibration

There are certain factors that have to be considered before performing the reflectance calibration. These factors include NIR noise and gamma correction, which are explained below.

4.3.2.1 NIR Noise

The PeauPro82 GoPro Hero 4 camera is equipped with an NDVI filter, which replaces the blue channel with the NIR channel. Theoretically, the red, green and NIR bands should be captured in their respective channels. However, since the red and green channels of PeauPro 82 cameras are extremely sensitive to the NIR band, they also tend to capture some NIR noise in them. In order to proceed with the calibration, the red band needs to be "cleaned" first. The following formula can be used for the noise cleaning:

$$I_{RC} = I_R - I_{NIR}\varepsilon \tag{12}$$

where ε is the percentage of NIR noise in the red channel and I_R, I_{NIR}, I_{RC} are the raw DNs of the noisy red band, NIR band and the "cleaned" red band respectively.

4.3.2.2 Gamma Correction

Gamma correction is a non-linear operation used to encode or decode the luminance in a video or a still image. The optical sensor non-linearizes the true luminance of the object in the image in order to produce a "pretty" picture, which can be perceived by the human eyes. The gamma correction formula is defined below:

$$I_{jpeg} = AI_{raw}^{\gamma}. \tag{13}$$

where I represents pixel intensity and γ represents the gamma correction scale.

The gamma correction needs to be removed in order to obtain a linear regression between the DNs and reflectance values, which is essential for the calibration.

4.3.2.3 Atmospheric Effects

The reflectance properties of an object at different spectral bands, depend largely on the atmospheric conditions. For instance, the NIR reflectance of an object on a humid day will be different as compared to a dry day. This is due to reflectance properties of water, as shown in Figure 31. Since water has a tendency to absorb NIR radiation, the NIR reflectance of any object on a humid day will be under predicted. The extent of under prediction of the NIR reflectance also depends on the distance between the sensor and the object. A direct consequence of this is inaccurate estimation of the NDVI. It is therefore important to gauge the atmospheric conditions before performing any calibration procedure.

4.3.3 NDVI Ground Test

A comprehensive ground test was performed using a PeauPro82 GoPro Hero 4 NDVI camera and the MAPIR reflectance ground target board (Figure 32) to test the calibration procedure. The test procedure is broken down into the following steps:

1. The MAPIR board is placed on the ground and a high-quality multispectral image is captured using the PeauPro82 GoPro Hero 4 NDVI camera as shown in Figure 34.
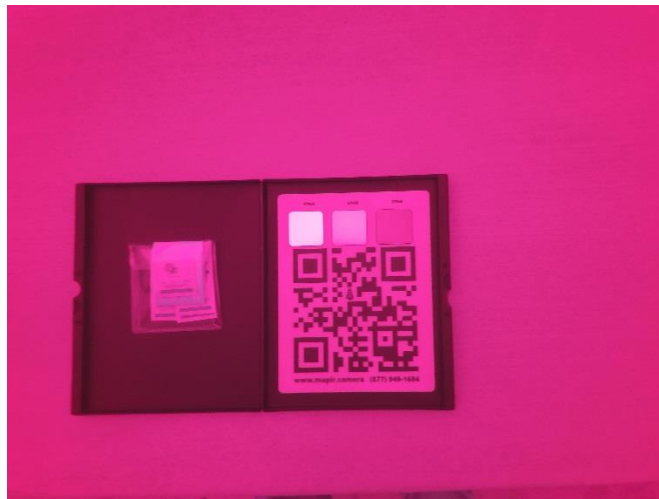
Figure 34. Ground image of the MAPIR ground target board.

2. At the same time, images of the surroundings are also captured to test the calibration procedure (Figure 35).

Figure 35. Ground test image.

3. The average DNs of the pixels corresponding to each surface on the target board are plotted with their respective reflectance values (Table 6) after applying the NIR noise filtration (Sec.4.4.2.1.)
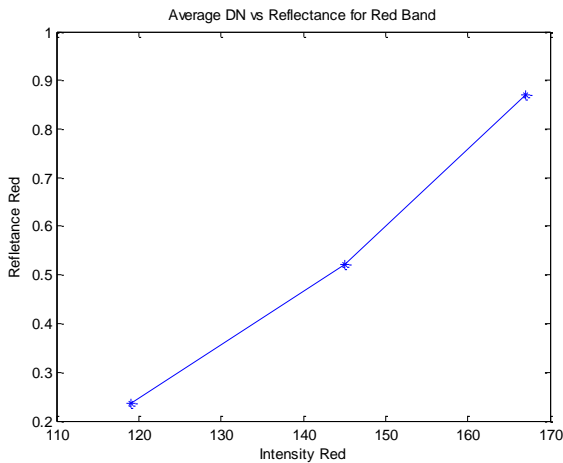
Figure 36. Average DN vs reflectance for red band before gamma re-correction.
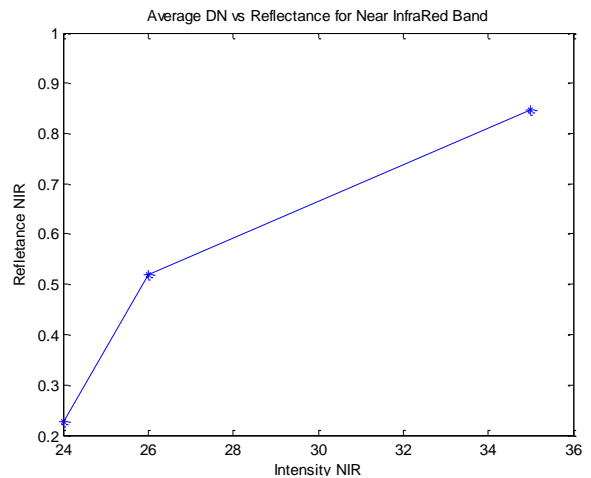
Figure 37. Average DN vs near infrared band before gamma re-correction.

4. It can be observed from Figure 36 and Figure 37 that the points do not form a linear relationship. This is due to the gamma correction. The next step in the calibration

41

procedure is the gamma re-correction which is performed using the algorithm presented below:

5. In order to have a linear regression between all the average DN values and reflectance, a gamma re- correction factor $\alpha = \frac{1}{\gamma}$ needs to be applied to the average DN values, where γ is the gamma correction factor. Given the theoretical reflectance values of the boards, R_1, R_2, R_3 and the average DNs of the jpeg image corresponding to each of these boards, I_1, I_2 and I_3 , the following can be formulated:

$$(R_2 - R_1)/ (R_3 - R_2) \ = \ (I_2^\alpha - I_1^\alpha)/(I_3^\alpha - I_2^\alpha) \tag{14}$$

Figure 38 and Figure 39 represent the linear regression between the average DN values and reflectance after performing gamma re-correction.
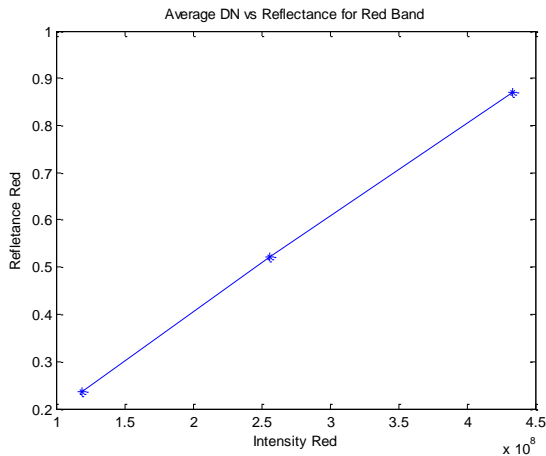
Figure 38. Average DN vs reflectance for red band after gamma re-correction.
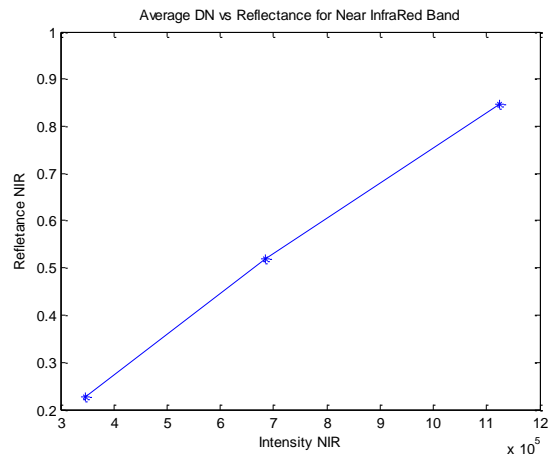
Figure 39. Average DN vs reflectance for near infrared band after gamma re-correction.

For further validation of the calibration procedure, a white board and a gray board with roughly known reflectance values were used (). The objective of this test was to test the identified linear relationship on other objects with different reflectance values and to prove the effectiveness of the proposed calibration procedure. Figure 41 and Figure 42 show the relationship between

DNs and corresponding reflectance values before gamma re-correction. Figure 44 and Figure 43 show the relationship after gamma re-correction.
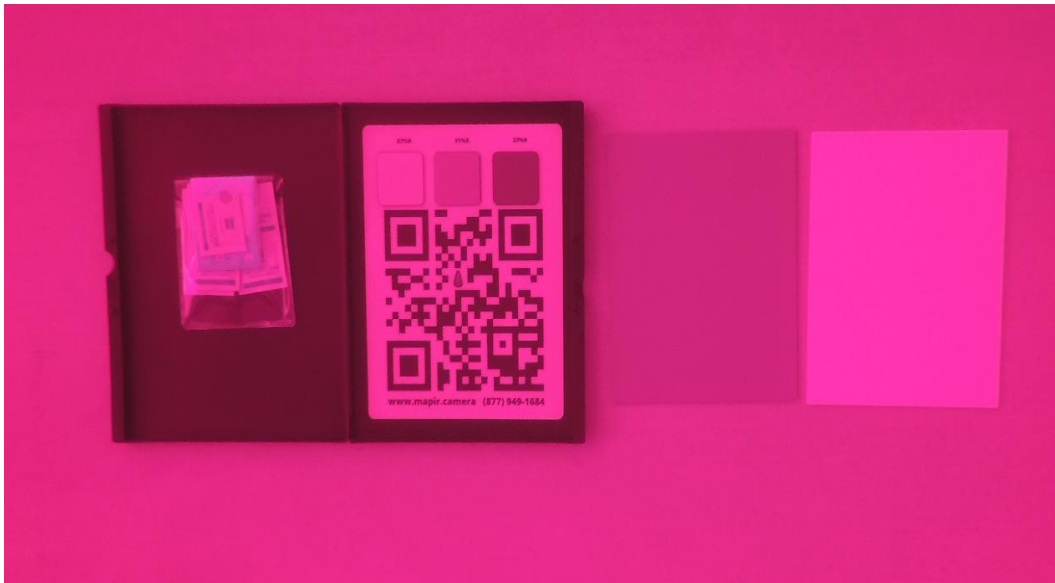
Figure 40. Ground image of the MAPIR ground target board plus white and white and gray boards (5-point test).
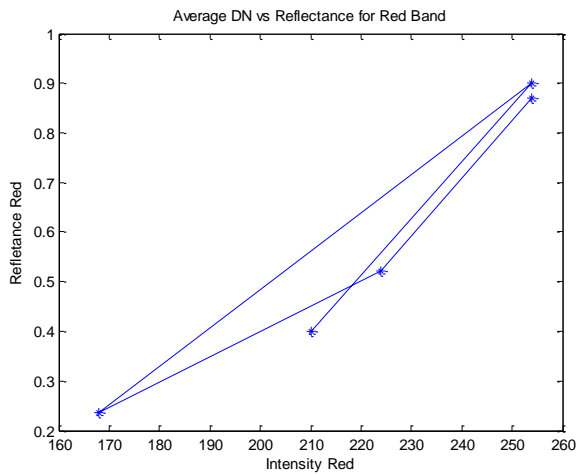
Figure 41. Average DN vs reflectance for red band before gamma re-correction (5-point test).
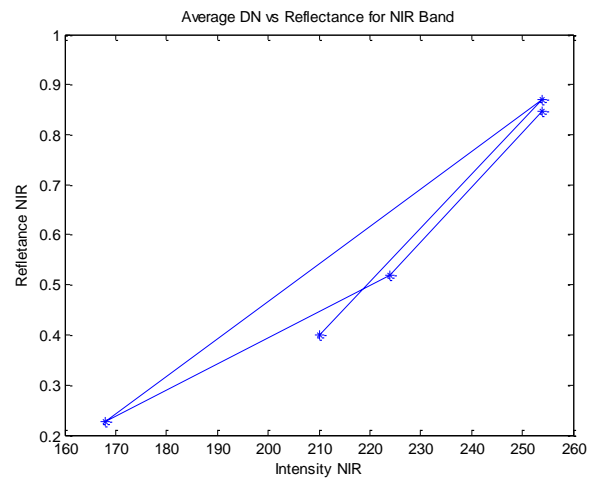
Figure 42. Average DN vs reflectance for NIR band before gamma re-correction (5-point test).
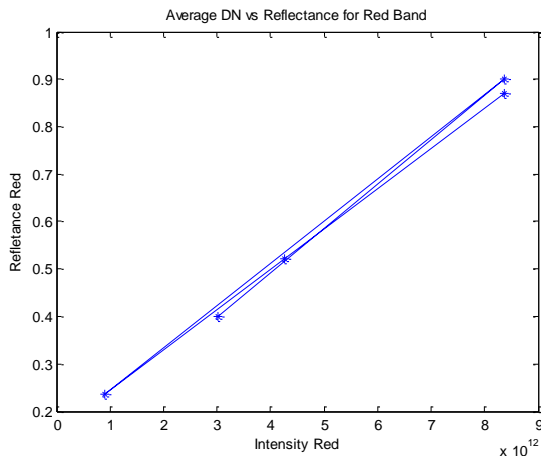
**Figure 44. Average DN vs reflectance for red band after gamma re-correction (5-point test).**
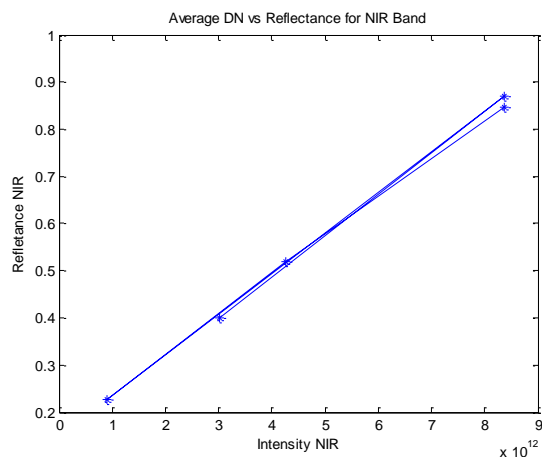
Figure 43. Average DN vs reflectance for NIR band after gamma re-correction (5-point test).

It can be observed that a linear regression is obtained after gamma re-correction. However, since the reflectance values of the included white and gray boards are guessed and are not accurate, small deviations can be noticed in the linear plots. It can be concluded that with known reflectance values, the NIR noise reduction and gamma re-correction procedures proposed in the above sections work with a target with other reflectance values.

Once the linear regression is established, the slopes and intercept values required for the global calibration is calculated and applied to all the pixel values in the test image. The calibration coefficients obtained from the procedure are applied to the test image and an NDVI raster calculation is made in order to validate the procedure. Figure 45 shows the NDVI false color image generated from the test image shown in Figure 35. It can be observed the NDVI values of the trees fall within their expected theoretical range of 0.6 - 0.9. An NDVI threshold image is also shown (Figure 46), which can be used for vegetation detection. The areas of NDVI values higher than 0.3 are highlighted.

44

Figure 45. NDVI false color image of ground test image.

Figure 46. NDVI threshold image for ground test image.

In order to further test the robustness of the calibration procedure, another ground test was performed on a different day with the raw image shown in Figure 47. Figure 48 and Figure 49 show the final NDVI false color image and the threshold images.
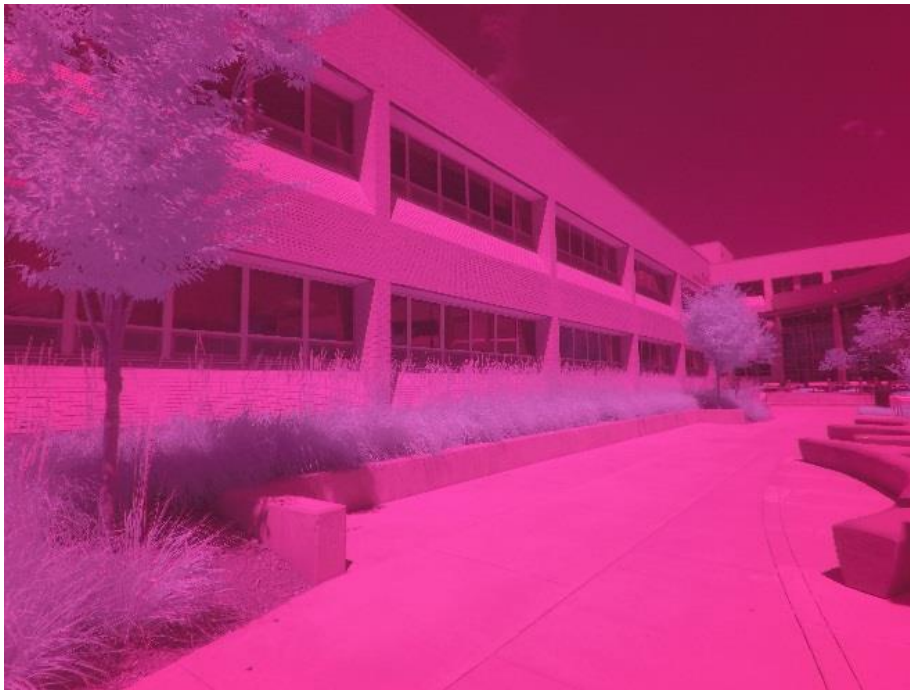
Figure 47.Ground Test image II.
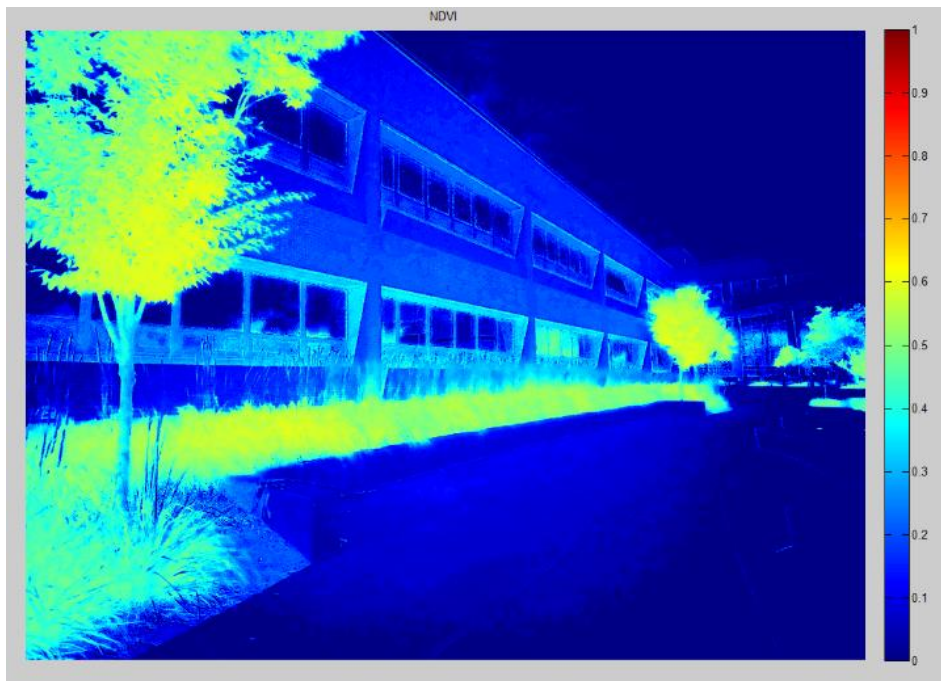
Figure 48. NDVI false color image of ground test image II.

Figure 49. NDVI threshold image of test image II.

Two interesting features can be observed in Figure 48, such as:

- The NDVI values of the top portion of the top grass are less than the values in the bottom.

- A particular window seems to show relatively higher NDVI values.

In order to understand these features, an RGB, red and NIR image of the same area were further shown in Figure 50 - Figure 52.

- The plants in the center seem to have a very low chlorophyll content in the top half, which justifies the feature observed in the NDVI image.

- The particular window in Figure 48 and Figure 49 with high NDVI values, was due to the reflection of the tree in front of it. It can be observed from Figure 51 and Figure 52 that this occurrence is due to effect of NIR reflectance.

Figure 50. RGB test image.

Figure 51. Test image - red.
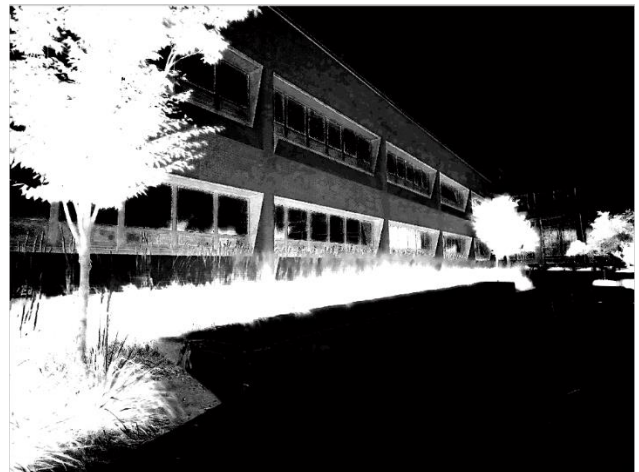
Figure 52. Test image - NIR band.

It can be concluded that the calibration procedure developed using MAPIR ground reflection ground target performs well and produces good results. In the next section, an implementation of this calibration procedure on real flight data is presented and discussed.

4.4 Flight Test Validation

The NDVI calibration procedure is further tested using KHawk flight data over the KU field station. The objective of this process is to compare our NDVI measurements with satellite NDVI values and ground NDVI values measured from a weather station. Figure 53 shows the NDVI false color map generated by the calibration equations obtained from the previous section.

KU Field Station
June 7,2017
Pixel Resolution : 0.12 m
NDVI map.
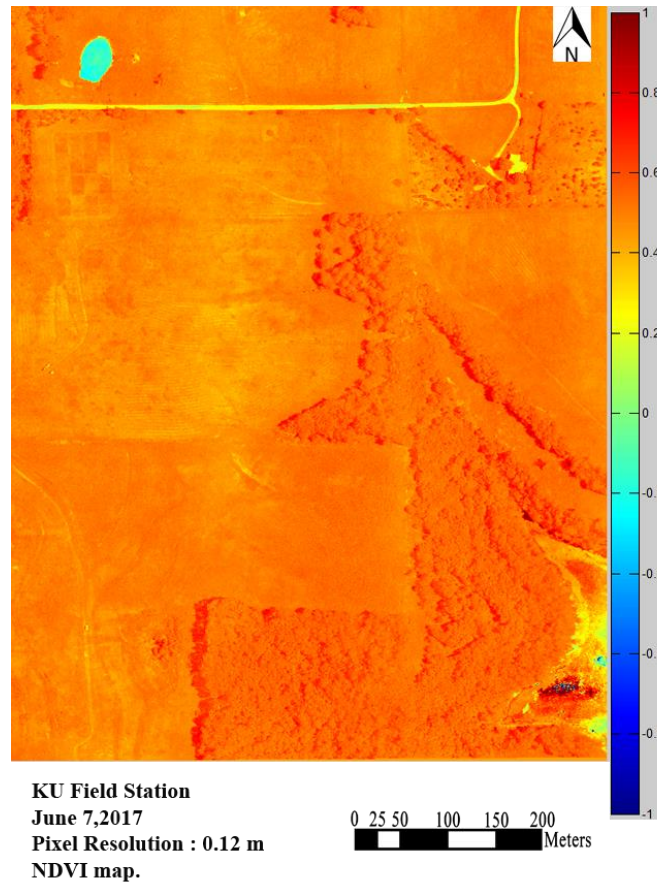
Figure 53. NDVI map post calibration.

Table 7 provides a comparison between the NDVI range as shown in Figure 53 and the theoretical NDVI range corresponding to certain objects.

Table 7. NDVI comparison.

Description	Theoretical NDVI range	Calculated NDVI mean
Dense Vegetation (trees, tropical plants)	0.6-0.9	0.58
Sparse Vegetation (shrubs, short grass)	0.2-0.5	0.38
Barren rock, sand, road	0-0.1	0.21
Water	< 0	<0

The reflectance values for the NIR band were plotted against those of the red band (Figure 54) corresponding the NDVI map shown in Figure 53.
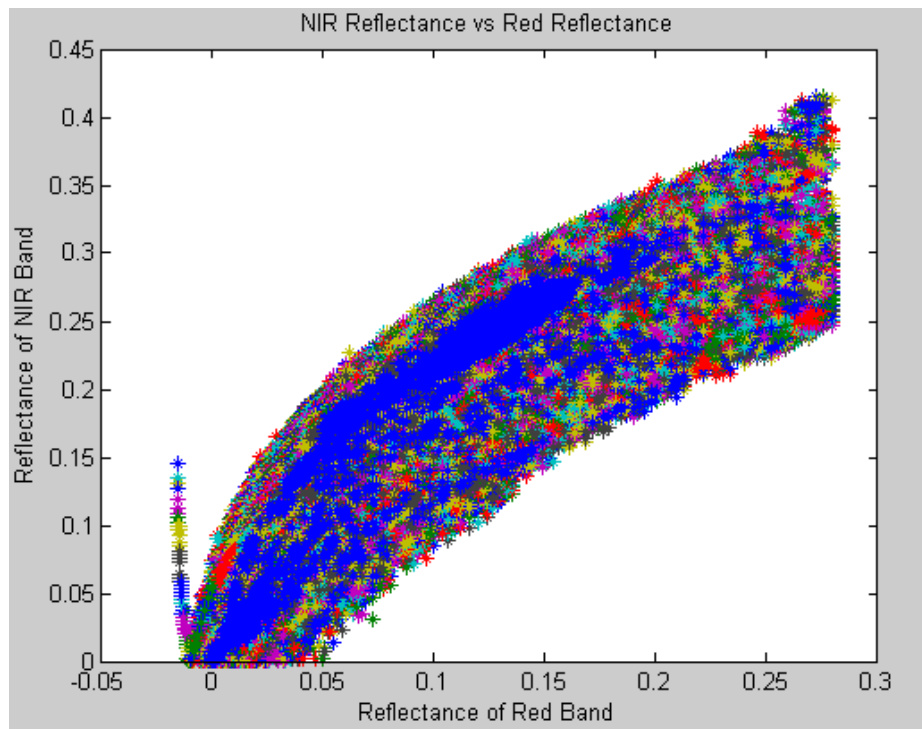
Figure 54. NIR reflectance vs red reflectance.

4.5 Chapter Summary

In this chapter, a multispectral aerial map generation method is introduced. Red, NIR and CIR band maps are presented and their significance is discussed. Next, the motivation for NDVI calibration is provided and a calibration procedure using MAPIR ground target reflectance boards is proposed. Further, two boards (white and gray) with predicted reflectance values are added to the existing MAPIR boards to prove that the proposed method can be extended to more than three points. Finally, ground tests and flight test validations for the proposed NDVI calibration procedure are presented.

5 Other Application Scenarios

This chapter focuses on two application scenarios, prescribed fire monitoring and tree height estimation. The first section provides a brief description of prescribed fire monitoring using KHawk aerial images and maps. The second section provides an introduction to tree height estimation using generated DEMs.

5.1 Prescribed Fire Monitoring

The major objectives of this section are to present the initial results for real-time monitoring of prescribed fires using KHawk UASs. The ultimate goal is to detect and estimate fire line location and magnitude throughout the burning. The KHawk UASs were flown over a prescribed fire at different burning stages. Aerial images and generated maps are used to determine the temporal and initial spatial characteristics of the fire. The prescribed fire was organized by the Kansas Biological Survey (KBS) crews at the KU field station as a routine method for controlling the vegetation. The GPS coordinates of the center for the burned area ($\sim 350 \times 170$ m) is 39.054131 degrees for latitude, and -95.189561 degrees for longitude. It was burned from 10:56 to 11:38 AM on April 7, 2017. The approximate start time of the fire was estimated based on the first sighting of fire/smoke on the video from the onboard camera on the first flight. Its corresponding frame was extracted and referenced with GPS and IMU data. With the knowledge of flight take-off time from flight log and the ITOW data from GPS, the approximate prescribed fire start time was calculated. The end-time was calculated based on the first sighting of dying fire/smoke from the video from the onboard camera on the third flight. Detailed temporal information for the prescribed fire can be found in Table 8.

Table 8. Temporal Characteristics of Fire.

Description	Time (Date:04/07/2017)
Fire Start Time	10:56:59 AM(CST)
Full Intensity Fire Time	11:32:44 AM (CST)
Fire End Time	11:38:06 AM (CST)
Approximate Duration of Fire	41 minutes 7 sec

5.1.1 KHawk Aerial Maps and Images

Two KHawk UASs were installed with the PeauPro82 GoPro Hero 4 RGB cameras and flown before, during and after the fire. Figure 55 shows the aerial map generated from the KHawk 48" UAS in the first flight, which was flown during the initial stages of the fire.

Figure 55. KHawk aerial map- initial stages of fire.

For the second flight, the KHawk 55" UAS was intentionally planned for image acquisition through the smokes, which can be observed from Figure 56 - Figure 58. Different phases of the fire can be seen from these figures. Note that manual mode was selected for this flight in consideration of the challenges coming from strong turbulence. A full site aerial map cannot be

obtained from the collected aerial images because of the challenges created by smokes, turbulence, and manual flight.

Figure 56.Pre-intense fire.

Figure 57. Full intensity fire.

Figure 58. Final stages of fire.

The KHawk 48" UAS was flown after the fire for the third flight to observe the effect of the fire on the field. The aerial map generated from this flight is shown in Figure 59.

Figure 59. KHawk aerial map- post fire.

Based on the collected aerial images and generated maps before, during and after the fire, an estimation of the fire line evolution pattern can be made. A comparison between the maps corresponding to the initial fire stage and post-fire stage can be made in order to determine the effect of the prescribed fire on the field.

5.2 Tree Health Monitoring

Another application of UAS based remote sensing is the estimation of DEM, which can be used to make measurements such as tree height, 3-D terrain distributions. KHawk aerial imagery was used to generate DEMs for the estimation of tree height.

A flight test was conducted on May 26, 2017 at the KU Field Station. The objective of this test was to estimate the height of trees using DEM. KHawk 48" UAS was installed with the PeauPro82 GoPro Hero 4 RGB camera and flown over selected trees. Figure 60 shows the RGB aerial map (left) and the DEM (right) generated from the collected aerial images.

The DEM provides the elevation data of the constructed map. It can be observed that an AGL scale of 307- 338 m was estimated, which can be correlated with the average AGL of the field obtained from Google Earth. The tree spatial pattern observed in the RGB aerial map and the DEM is in agreement, which provides another validation to the DEM. The average height of the

tree line is estimated to be 12-15 m. The major advantage of using DEMs for tree health estimation, is that it can also provide 3D spatial information and the canopy height distribution of the trees.
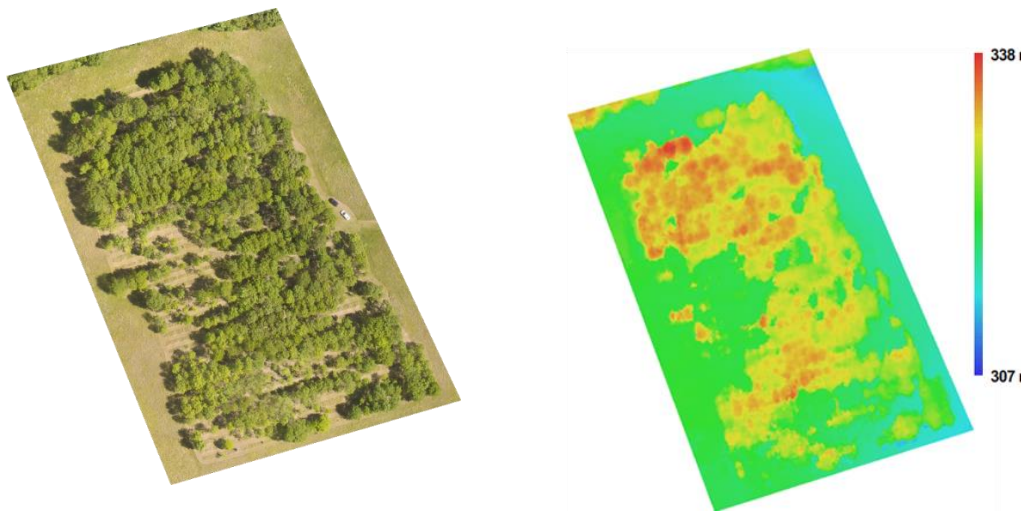
Figure 60. KHawk aerial map of tree line (left: RGB, right: DEM).

5.3 Chapter Summary

In this chapter, the use of KHawk aerial imagery in fire monitoring and fire line estimation is proposed and discussed. The temporal characteristics of the fire are estimated based on time stamps on the geotagged aerial images and aerial maps. The approximate duration of the prescribed fire is calculated to be 41 minutes and 7 seconds. The aerial images and generated maps from the three KHawk UAS flights are presented. Next, the application of DEMs generated from KHawk aerial maps for tree health estimation is presented. A constructed DEM of a tree line is presented along with its corresponding RGB aerial map. The average height of the trees from the DEM is estimated to be 12-15 m.

6 Conclusions and Recommendations

6.1 Conclusions

In summary, the KHawk aerial map generation procedure is proposed and validated using collected aerial data. For the current system, KHawk UAS can generate multispectral aerial maps of a coverage area of 5 km×5 km with an accuracy of less than 10 m for one flight. The KHawk 48" UAS can achieve a pixel resolution of 0.10 - 0.12 m at a flying altitude of 120 m using PeauPro82 GoPro Hero 4 cameras (RGB/NIR). The proposed methods for multispectral aerial mapping and NDVI calibration prove to be effective for vegetation detection and crop analysis. The KHawk remote sensing procedures system is further tested in applications such as prescribed fire monitoring, fire line estimation and tree health monitoring.

6.2 Recommendations

The future recommendations regarding the use of KHawk UAS for remote sensing can be summarized as follows:

- Replacement of compact video cameras with high resolution digital cameras such as Canon Powershot S100;

- Inclusion of spectrometer on-board the UAS for true spectral reflectance measurements;

- Inclusion of hyperspectral cameras (Mica Sense) for more applications;

- The implementation of thermal cameras for temperature analysis;

- Real time aerial video viewing capability.

References

[1]   Steve Graham, *Remote Sensing*, NASA Earth Observatory, 1999.

[2]   Paul R. Baumann, *History of Remote Sensing, Aerial Photography*, Oneonta, New York, 2014.

[3]   Department of Geography, "Multispectral Remote Sensing Systems", Penn State College of Earth and Mineral Sciences, 2009.

[4]   "Vegetation Index", [https://en.wikipedia.org/wiki/Vegetation_Index].

[5]   "Normalized Difference Vegetation Index", [https://en.wikipedia.org/wiki/Normalized_Difference_Vegetation_Index].

[6]   "Soil-Adjusted Vegetation Index", [https://en.wikipedia.org/wiki/Soil-Adjusted_Vegetation_Index].

[7]   "Enhanced Vegetation index", [https://en.wikipedia.org/wiki/Enhanced_vegetation_index].

[8]   "Unmanned Aerial Vehicle", [https://en.wikipedia.org/wiki/Unmanned_aerial_vehicle].

[9]   "Lidar", [https://en.wikipedia.org/wiki/Lidar].

[10]   "Synthetic -aperture Radar", [https://en.wikipedia.org/wiki/Synthetic-aperture_radar].

[11]   Precision Hawk Company, [http://www.precisionhawk.com/lancaster].

[12]   Precision Hawk Company, [http://www.precisionhawk.com/].

[13]   AggieAir, "Minion 2.0", [http://aggieair.usu.edu/node/349].

[14]   AggieAir, [http://aggieair.usu.edu/].

[15]   Trimble Company, [http://uas.trimble.com/ux5].

[16]   Trimble Company, [http://www.trimble.com/].

[17]   UASUSA Company, [http://www.uasusa.com/].

[18] UASUSA Company, "The Tempest", [http://www.uasusa.com/products-services/aircraft/the-tempest.html].

[19] A. T. Rua, M. A. Arab, L. H. Esfahani, A. Jensen and M. Mckee, "Development of Unmanned Aerial Systems for Use in Precision Agriculture: The AggierAir Experience", in *Proceedings of the 2015 IEEE Conference on Technologies for Sustainability*, August 2015.

[20] H. Chao, M. Baumann, A. Jensen, Y. Chen, Y. Cao, W. Ren, M. Mckee, "Band-reconfigurable Multi-UAV-based Cooperative Remote Sensing for Real-time Water management and Distributed Irrigation Control", in *Proceedings of the 2008 International Federal of Automatic Control World Conference (IFAC)*, pp. 11 744 -11 749, July 2008.

[21] K. Pauly, "Applying conventional vegetation vigor indices to UAS-derived orthomosaics: issues and considerations", in *Proceedings of the International Society of Precision Agriculture (ICPA)*, 2014.

[22] B. Stark , T, Zhao and Y. Chen, "An Analysis of the Effect of the bi-directional reflectance distribution function on remote sensing imagery accuracy from small Unmanned Aircraft Systems", in *Proceedings of the International Conference of Unmanned Aircraft Systems (ICUAS)*, 2016.

[23] B. Zaman, A. Jensen, S.R. Clemens and M. Mckee , " Retrieval of Spectral reflectance of high resolution multispectral imagery acquired with an autonomous unmanned aerial vehicle :AggieAir" , *American Society for Photogrammetry and Remote Sensing* , vol.80, no.12, pp. 1139-1150, December 2014.

[24] D. W. Casbeer, S.M Li, R.W. Beard, T.W. McLain and R.K. Mehra ,"Forest Fire Monitoring With Multiple Small UAVs", in *Proceedings of the 2005 American Control Conference*, pp. 3530 – 3535, June 2005.

[25] P. B. Sujith, D. Kingston., and R.W. Beard, "Cooperative Forest Fire Monitoring using Multiple UAVs", in *Proceedings of the 46th IEEE Conference on Decision and Control*, December 2007.

[26] A. E. Ononye, A. Vodacek and E. Saber, "Automatic Extraction of fire line parameters from multispectral infrared images", *Remote Sensing of Environment*, vol.108, September 2006.

[27] A. C. Birdal, U. Avdan and T. Turk, "Estimating tree heights with images from an unmanned aerial vehicle", *Informa UK Limited, trading as Taylor & Francis Group*, 2017.

[28] A. Jensen ,Y. Han and Y. Chen , "Using Aerial Images to Calibrate the Inertial Sensors Of a Low cost multispectral autonomous remote sensing platform (AggieAir)", in *Proceedings of the IEEE International Geoscience and Remote Sensing Symposium (IGARSS)* ,2009.

[29] "Remote Sensing", [https://en.wikipedia.org/wiki/Remote_sensing].

[30] Peau Productions Company, [https://www.peauproductions.com/products/peaupro82].

[31] "Photogrammetry", [http://www.photogrammetry.com/].

[32] "Photogrammetry", [https://en.wikipedia.org/wiki/Photogrammetry].

[33] Mathworks , "Camera Calibration" , [https://www.mathworks.com/help/vision/camera-calibration.html].

[34] "Reprojection Error", [https://en.wikipedia.org/wiki/Reprojection_error].

[35] H. Chao, "Cooperative Remote Sensing and Actuation using networked Unmanned Vehicles", Ph. D Dissertation, Utah State University, 2010.

[36] Agisoft Company, [http://www.agisoft.com/], 2017.

[37] Alchetron, [https://alchetron.com/PhotoScan-4138319-W].

[38] Minnesota IT Services, *Color-Infrared (CIR) Imagery,* [http://www.mngeo.state.mn.us/chouse/airphoto/cir.html]

[39] USGS, "Remote Sensing Phenology", [https://phenology.cr.usgs.gov/ndvi_foundation.php], January 2015.

[40] J. Weier and D. Herring, *Measuring Vegetation (NDVI &EVI),* NASA Earth Observatory, 2000.

[41] MAPIR Company, [https://www.mapir.camera/products/mapir-camera-calibration-ground-target-package].

[42] SEOS, "Introduction to Remote Sensing", [http://www.seos-project.eu/modules/remotesensing/remotesensing-c00-p01.html].

[43] Y. Han, "An Autonomous Unmanned Aerial Vehicle –Based Imagery system development and remote sensing images classification for agricultural applications", Master's Thesis, Utah State University, 2009.

[44] A. S. Laliberte, M. A. Goforth, C.M. Steele and A. Rangs, "Multispectral remote sensing from Unmanned aircraft: Image processing workflow and Applications for Rangeland Environments", *Journal of Remote Sensing, MDPI*, November 2011.

[45] P. J. Hardin and R. R. Jensen, "Small –scale unmanned aerial vehicles in environmental remote sensing: Challenges and opportunities", *GIScience & Remote Sensing*, no.1, p. 99-111, 2011.

[46] N. Horning, [https://publiclab.org/tag/calibrate-ndvi].

[47] H. Chao, Y, Gu and M. Napolitano, "A Survey of Optical Flow Techniques for Robotics Navigation Applications", in *Proceedings of the 2013 International Conference on Unmanned Aircraft Systems (ICUAS),* May 2013.

[48] UTSA, *Intro to Remote Sensing,* 2005.

[49] H. Chao, Y. Chen, *Remote Sensing and Actuation using Unmanned Vehicles,* Wiley-IEEE Press, August 2012.